
Supporting Information

Exploring Zn-Regulated Function in Co-Zn Catalyst for Efficient Hydrogenation of Ethyl Levulinate to γ-Valerolactone

Jie Chu,[a] *Yafei Fan,*[a] *Lu Sun,*[a] *Ying Wang,*[a] *Yunxian Li,*[a] *Xiaoqin Zou,*[b*] *Chungang Min,*[c*] *Terence Xiaoteng Liu,*[d] *Changfu Zhuang,*[a*] *Guangshan Zhu*[b]

[a] Key Laboratory of Forest Resources Conservation and Utilization in the Southwest Mountains of China Ministry of Education, School of Chemical Engineering, Southwest Forestry University, Kunming 650051, P. R. China.

[b] Faculty of Chemistry, Northeast Normal University, Changchun 130024, P. R. China.

[c] Research Center for Analysis and Measurement, Kunming University of Science and Technology, Kunming 650093, P. R. China.

[d] Department of Mechanical and Construction Engineering, Faculty of Engineering and Environment, Northumbria University, Newcastle upon Tyne, NE1 8ST, United Kingdom.

* *Corresponding Authors*

E-mail: cfzhuang@swfu.edu.cn (Changfu Zhuang); E-mail: zouxq100@nenu.edu.cn (Xiaoqin Zou); E-mail: minchungang@163.com (Chungang Min)

Additional Experimental Details and Methods

Effect of Reaction Conditions

To obtain the optimum experimental conditions on Hydrogenation of EL to GVL, a series of experiment was conducted and shown in Figure S11. From Figure S11a it can be seen that the EL conversion increased along with increasing reaction temperature, and reached an optimum value (>99%) at 140 ℃. Further elevating the reaction temperature to 150 ℃, GVL yield decreased because of the reduction of selectivity. The effect of time on the yield of GVL (Figure S11b) was investigated at the temperature of 140 ℃. EL conversion and GVL yield continuously increased and reached the maximum value (>99%) at 4 h. However, GVL yield exhibited a declining trend once the reaction time longer than 4 h, which could be ascribed to the side reaction. Figure S11c presents the effect of H_2 pressure intensity on EL conversion. With the increase of pressure intensity from 1 MPa to 2 MPa, the upward trend of EL conversion was found with that of GVL yield. Further increase the pressure intensity could not improve the catalytic results but lead to a slightly decrease. Thus, the optimal pressure intensity of H_2 was 2 MPa.

In order to determine the optimal solvent and dosage for EL catalytic hydrogenation, we also tested the performance of hydrogen solvent on GVL yield (Figure S11d). Following the order of THF < 2-butanol < EAC < n-butanol < n-propanol < methanol < ethanol < 2-propanol, GVL yield increased significantly from 6.8% to >99%. Among various solvents, 2-propanol can obtain the best catalytic effect (GVL yield >99%), indicating secondary alcohols were most effective for hydrogenation of EL due to their lower reduction potential. As for the influence of solvent dosage, 2-propanol with different doses (6, 8, 10, 12 and 14 mL) was added to participate in the reaction, and the GVL yield reached an optimum value (>99%) at 8 ml. Besides, it is worth mentioning that 2-propanol can act as the hydrogen source (without H_2 and using N_2 as protecting gas) and the GVL yield given a value of 21.99% (160 ℃). When the reaction temperature reduced from 160 to 140 ℃, the catalytic transfer hydrogenation was so weak that can be neglect, and the reaction was mainly due to the action of H_2.

Effect of Pyrolysis Temperature

1. Effects of Pyrolysis Temperature on Catalyst Characterization

The pyrolysis temperature plays a significant role in the micro-structure of Co_3Zn_1@NPC-T. As shown in Figure S2, the average particle size of metal particles increases with the rising temperature, accompanied by more uneven particle size distribution. The particle size is relatively uniform (from 11.3 to 11.9 nm) at the calcination temperature between 500 and 600 ºC. But the agglomeration became severe at 700 and 800 ºC, inducted size increase to 17.2 and 18.2 nm (Figure S3).

It was observed that the Co content changes irregularly with increasing temperature for Co_3Zn_1@NPC-T (Figure S5). The Co(0) content first increase from 25.83% (Co_3Zn_1@NPC-500) to 66.20% (Co_3Zn_1@NPC-600), then decrease to 28.44% (Co_3Zn_1@NPC-800). Co_3Zn_1@NPC-600 possesses the highest Co(0) content (66.20%), while Co_3Zn_1@NPC-500 has the lowest Co(0) content (25.83%) (Table 1). This is because Co_3Zn_1-ZIF precursors are relatively stable at 500 ºC and most Co content couldn't be reduced to metallic Co, consistent with the TG result in Figure S10.

In figure S7, Co_3Zn_1@NPC-T samples have the same XRD peak profile, but with calcination temperature increased from 500 to 800 ºC, the peak width becomes narrower and peak intensity goes stronger. The result suggests an increased size of metal NPs in Co_3Zn_1@NPC-T materials with the increased pyrolysis temperature, consistent with the change of size distributions from former TEM analysis (Figure S2 & Figure S3).

The pore structure of materials also varies dramatically according to the pyrolysis temperature (Figure S8). With the raising temperature, the surface area increased from 244 m^2 g^{-1} (Co^3Zn^1@NPC-500) to 343 m^2 g^{-1} (Co^3Zn^1@NPC-600), then decreased to 236 m^2 g^{-1} (Co^3Zn^1@NPC-800). Pore volume and metal particle size of Co^3Zn^1@NPC-T shows similar tendency (Table 1), that they all increase obviously with the raise of temperature. Among the catalysts, Co_3Zn_1@NPC-600 has a medium and appropriate porous structure (the surface area is 343 m^2 g^{-1}, pore volume is 0.27 cm^3 g^{-1}, metal particle size is 11.9 nm).

2. Effects of Pyrolysis Temperature on the EL Hydrogenation Reaction

The morphology, structure and composition of Co_xZn_y@NPC-T catalysts would be changed by pyrolysis temperature, thus affecting their catalytic hydrogenation results. So, the performance of Co_xZn_y-ZIFs pyrolyzed at different temperature (500, 600, 700 and 800 ^oC) is further investigated in our study. Among various catalysts, Co_3Zn_1@NPC-600 has the optimal catalytic performance with >99% EL conversion and >99% high GVL selectivity (Table 2, Entry 5). On the contrary, the Co_3Zn_1@NPC-500 only gives 55.5% GVL yield (Table 2, Entry 9). These results can be explained as follows: (1) Co_3Zn_1@NPC-500 has the lowest 15.83% of Co(0) content (Table 1, Entry 8); (2) The surface area of Co_3Zn_1@NPC-500 is much lower than Co_3Zn_1@NPC-600 (244 $m^2\ g^{-1}$ vs. 343 $m^2\ g^{-1}$) (Table 1), which is adverse for the exposure of active sites. Co_3Zn_1@NPC-700 has a yield of 89.3% (Table 2, Entry 10) lower than Co_3Zn_1@NPC-600, which could be ascribed to the lower Co(0) content (40.24%, Table 1), lower surface area (285 $m^2\ g^{-1}$, Table 1) and much larger NPs size (17.2 nm, Figure S3c) of Co_3Zn_1@NPC-700. The agglomeration of metal NPs will get serious when the calcination temperature increases too high, which led to a reduction in conversion of EL. Especially, Co_3Zn_1@NPC-800 catalysts with the largest particle sizes (18.2 nm, Table 1), meet a sharp drop in yield to 60.7% (Table 2, Entry 11). Therefore, it can be summarized that the pyrolysis temperature of precursor play a crucial role in the activity of Co_xZn_y@NPC-T by influencing its active Co(0) content, pore structure and metal NPs size.

For all these analyses, a conclusion can be drawn that the pyrolysis temperature, along with the Zn content, both play crucial roles in the improvement of Co_xZn_y@NPC-T catalysts.

Computational Method.

All calculations were performed using the Vienna ab initio simulation package (VASP) with the DFT method.[1, 2] The generalized gradient approximation of Perdew–Burke–Ernzerhof (PBE) was used to describe the exchange-correlation.[3] Meanwhile, the van der Waals interactions have been accurately described using the DFT-D3 method.[4] The cut-off energy for the plane wave basis set was 400 eV and the ionic positions of all structures were relaxed until the force converged to below -0.03 $\mathrm{eV \cdot Å^{-1}}$. A k-point mesh of gamma-centered 3 × 3 × 1 set was adopted. The vacuum between slabs along the *z*-direction was set at a minimum of 15 Å to minimize interactions between the slabs and reduce the complexity of the calculation.

The adsorption energy (E_{ads}) of EL and H_2 was defined as the formula

$$E_{ads} = E_{total} - (E_{slab} + E_g) \tag{3}$$

where E_{total} is the total energy after adsorption; E_{slab} is the energy of the clean slab alone, E_g is the energy of EL or H_2 in the gas phase, respectively.

Additional Preparation Method

Preparation of Co_3Zn_1@NPC-600(NH_4Cl): 0.1 g Co_3Zn_1@NPC-600 and 0.3 g NH_4Cl were fully grinded in the agate mortar to form a homogenous mixture. Subsequently, the mixture was placed into a tube furnace for pyrolysis at 350 °C for 48 h in Ar flow to remove metal NPs. The treated sample was cooled to room temperature, washed with distilled water for several times and then dried in vacuum at 80 °C for overnight, which was denoted as Co_3Zn_1@NPC-600(NH_4Cl).

Supplementary Figures

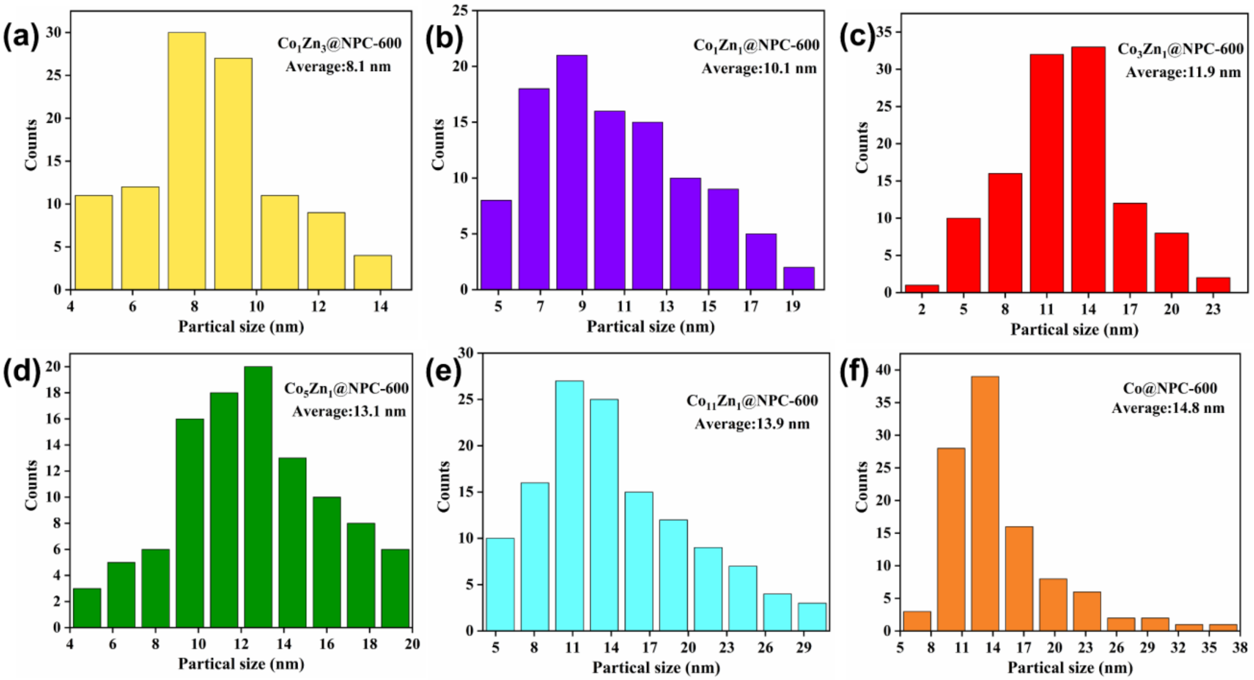

Figure S1. The particle sizes distribution of (a) Co_1Zn_3@NPC-600, (b) Co_1Zn_1@NPC-600, (c) Co_3Zn_1@NPC-600, (d) Co_5Zn_1@NPC-600, (e) $Co_{11}Zn_1$@NPC-600 and (f) Co@NPC-600.

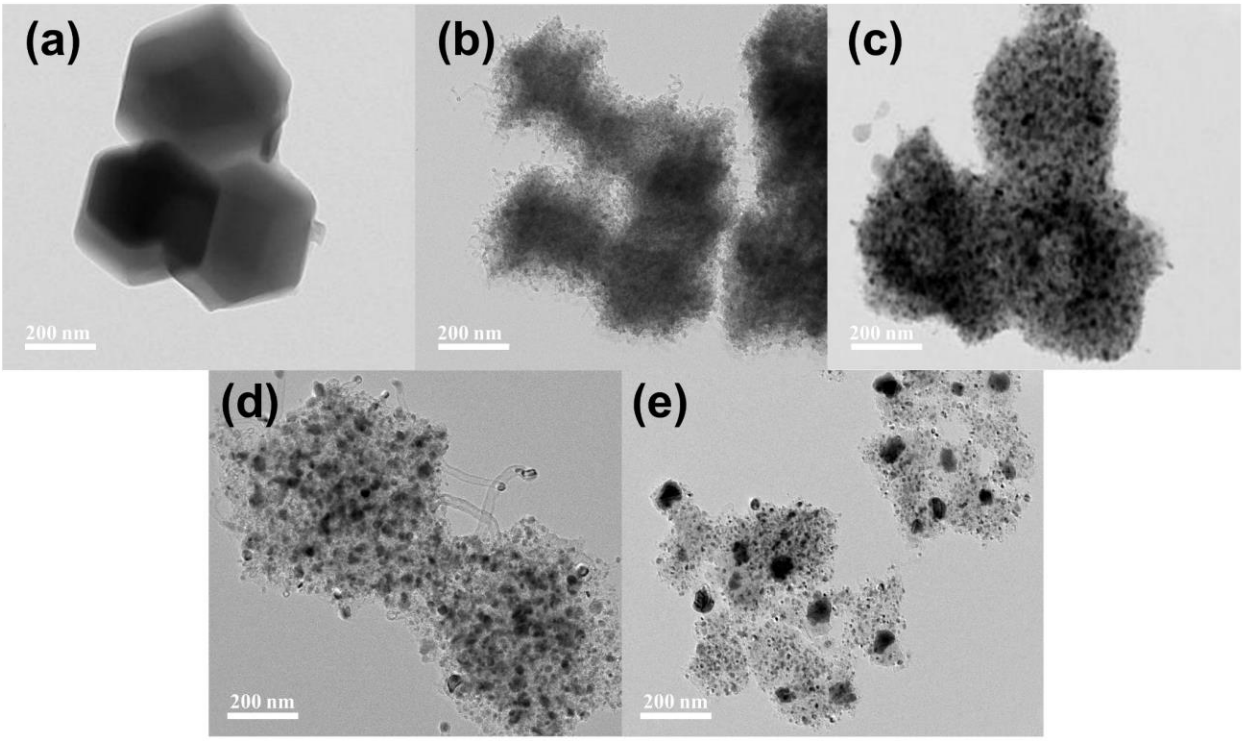

Figure S2. TEM images of (a) Co_3Zn_1-ZIFs, (b) Co_3Zn_1@NPC-500, (c) Co_3Zn_1@NPC-600, (d) Co_3Zn_1@NPC-700 and (e) Co_3Zn_1@NPC-800.

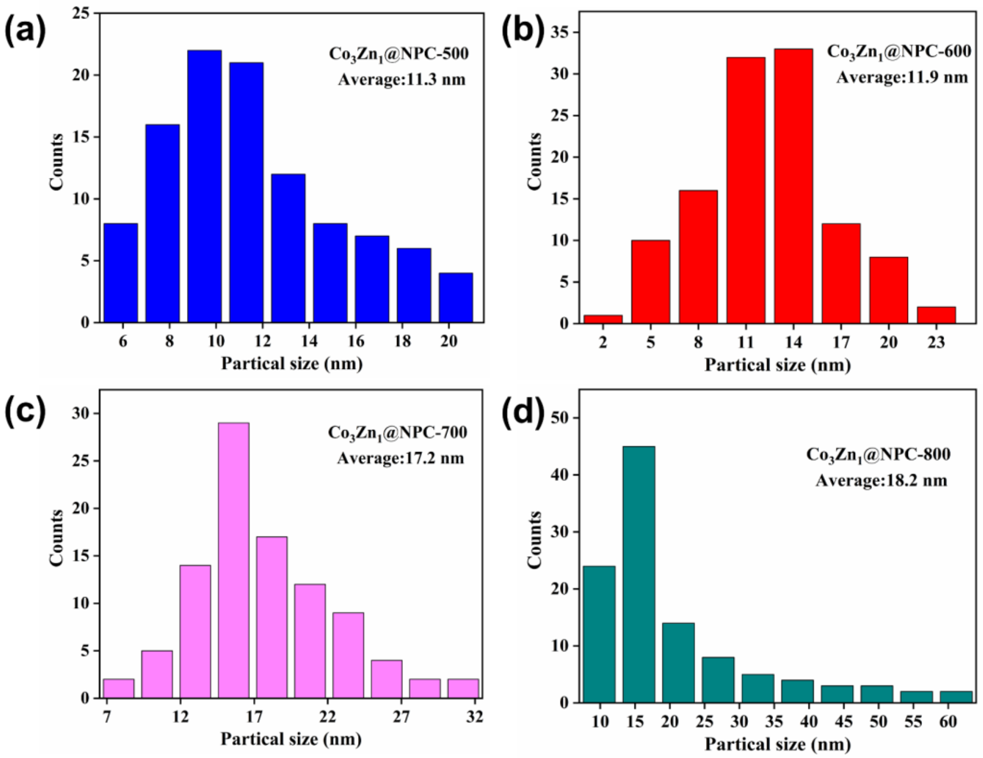

Figure S3. The particle sizes distribution of (a) Co_3Zn_1@NPC-500, (b) Co_3Zn_1@NPC-600, (c) Co_3Zn_1@NPC-700 and (d) Co_3Zn_1@NPC-800.

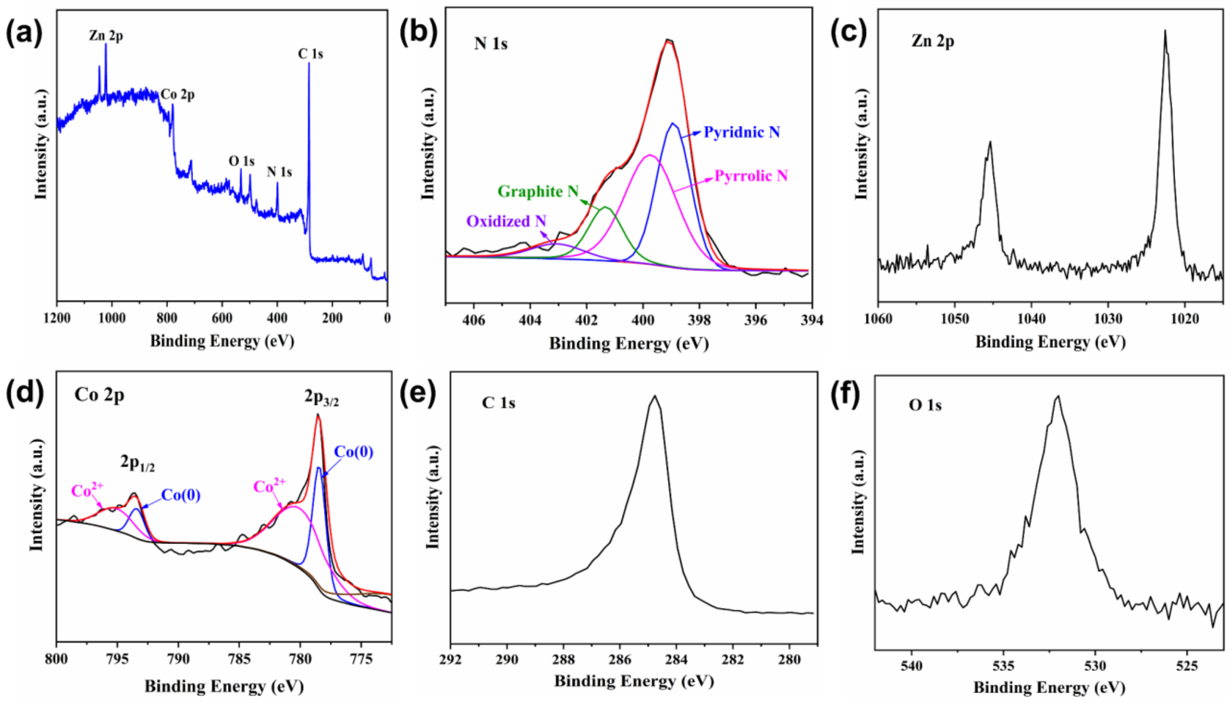

Figure S4. XPS spectra of Co_3Zn_1@NPC-600 materials, (a) full spectrum, (b) N 1s, (c) Zn 2p, (d) Co 2p, (e) C 1s and (f) O 1s.

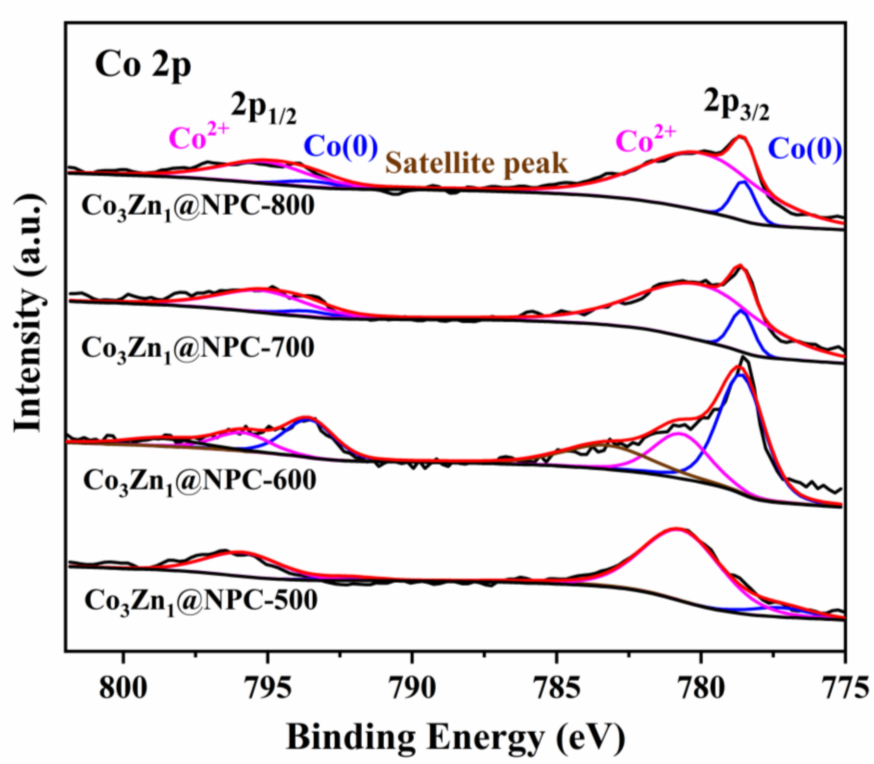

Figure S5. XPS spectra of Co 2p for Co_3Zn_1@NPC-T.

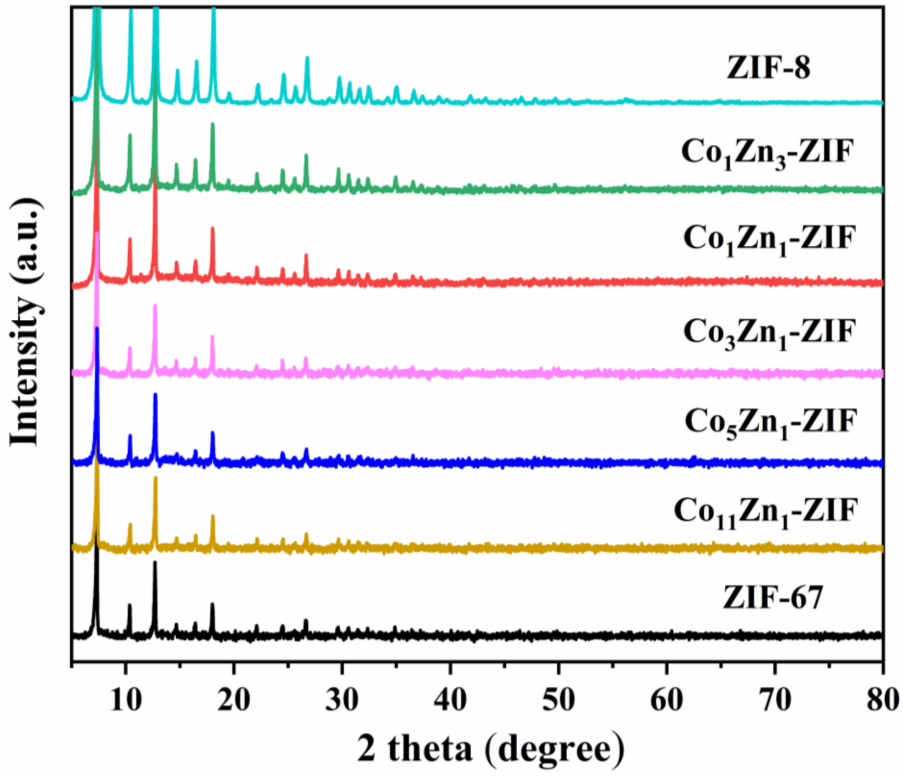

Figure S6. Powder XRD patterns of ZIF-8, ZIF-67 and a series of BMZIFs.

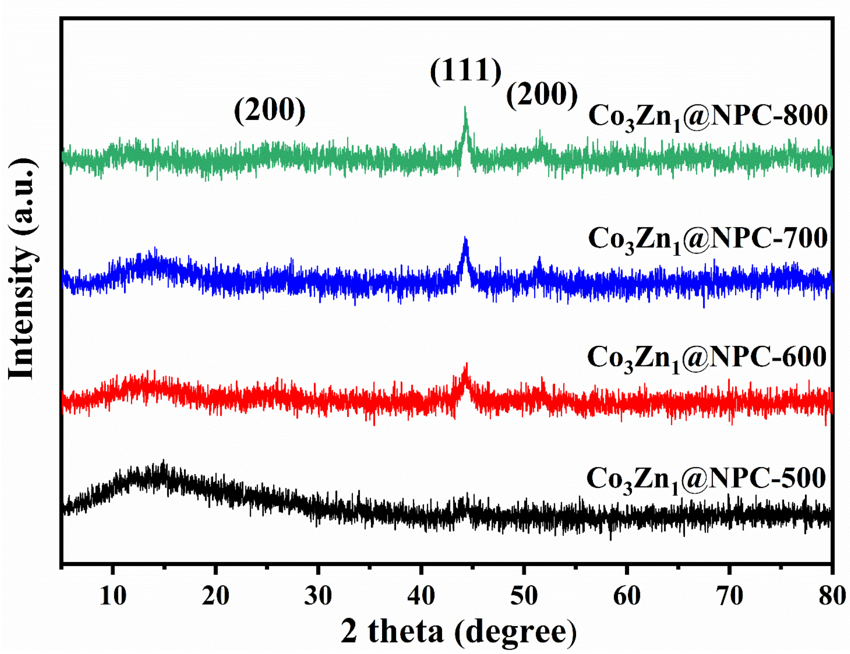

Figure S7. XRD patterns of the Co_3Zn_1@NPC-T materials (from 500 to 800 °C).

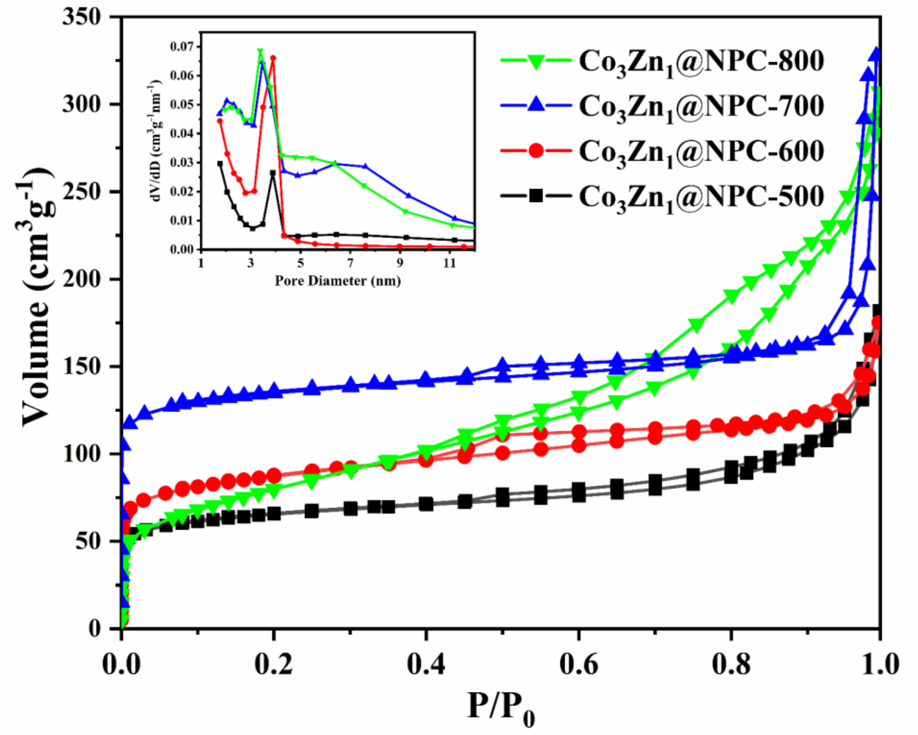

Figure S8. N_2 adsorption-desorption isotherms and the pore size distribution (inset) of the Co_3Zn_1@NPC-T materials.

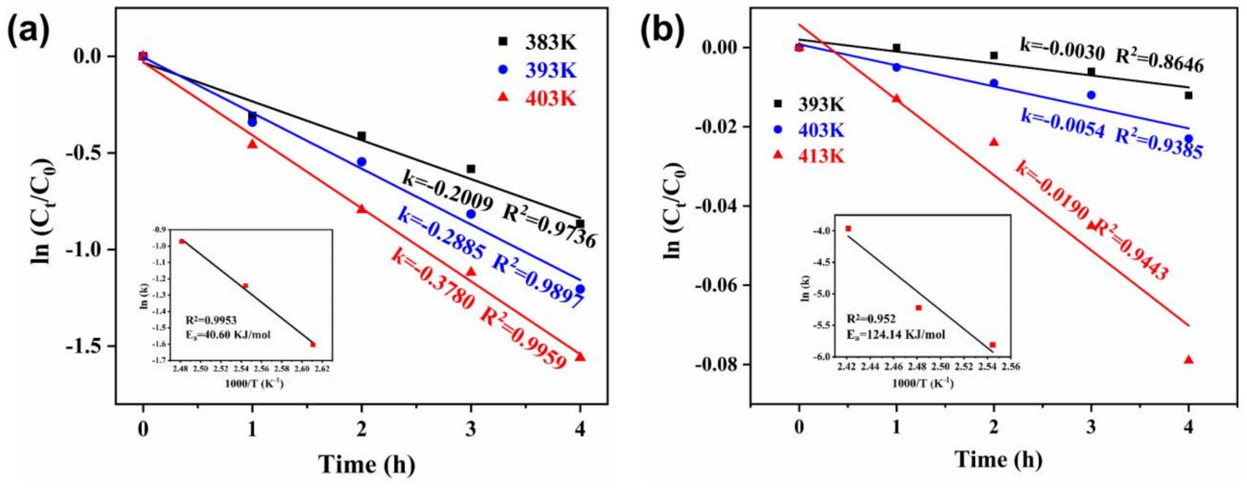

Figure S9. Kinetic studies of EL hydrogenation over (a) Co_3Zn_1@NPC-600 and (b) Co@NPC-600 at different temperatures (the inset represents the Arrhenius plot for the EL hydrogenation). Reaction conditions: 1 mmol EL, 0.025 g catalyst, 8 mL 2-propanol, 2 MPa H_2, 110-140 ℃.

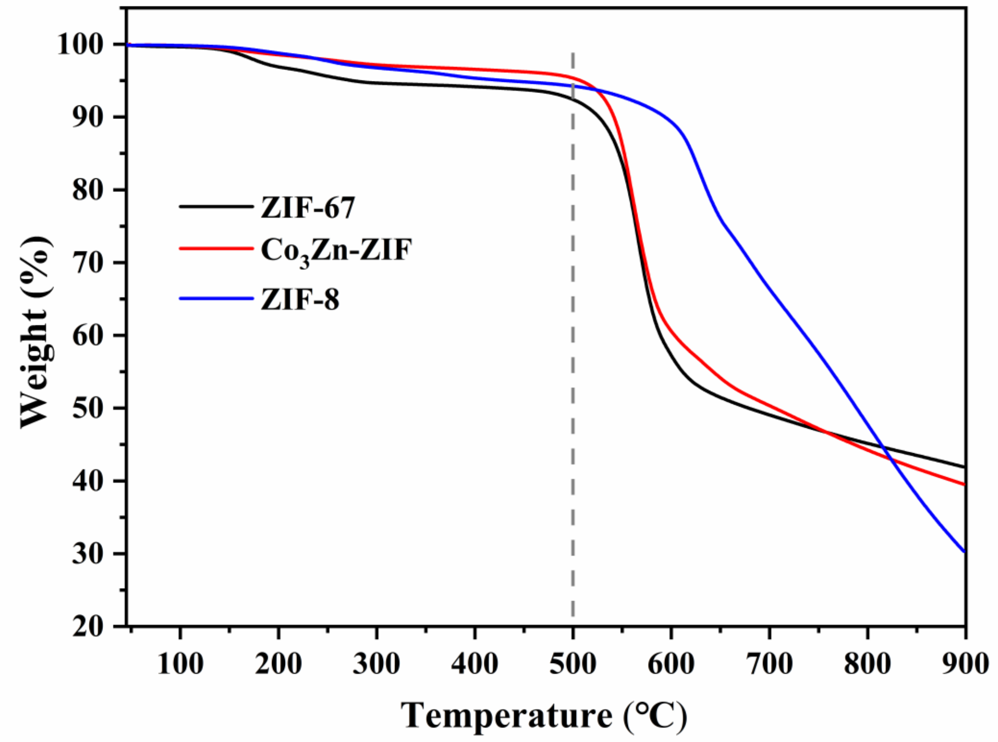

Figure S10. TG curves of ZIF-67, Co_3Zn_1-ZIF and ZIF-8.

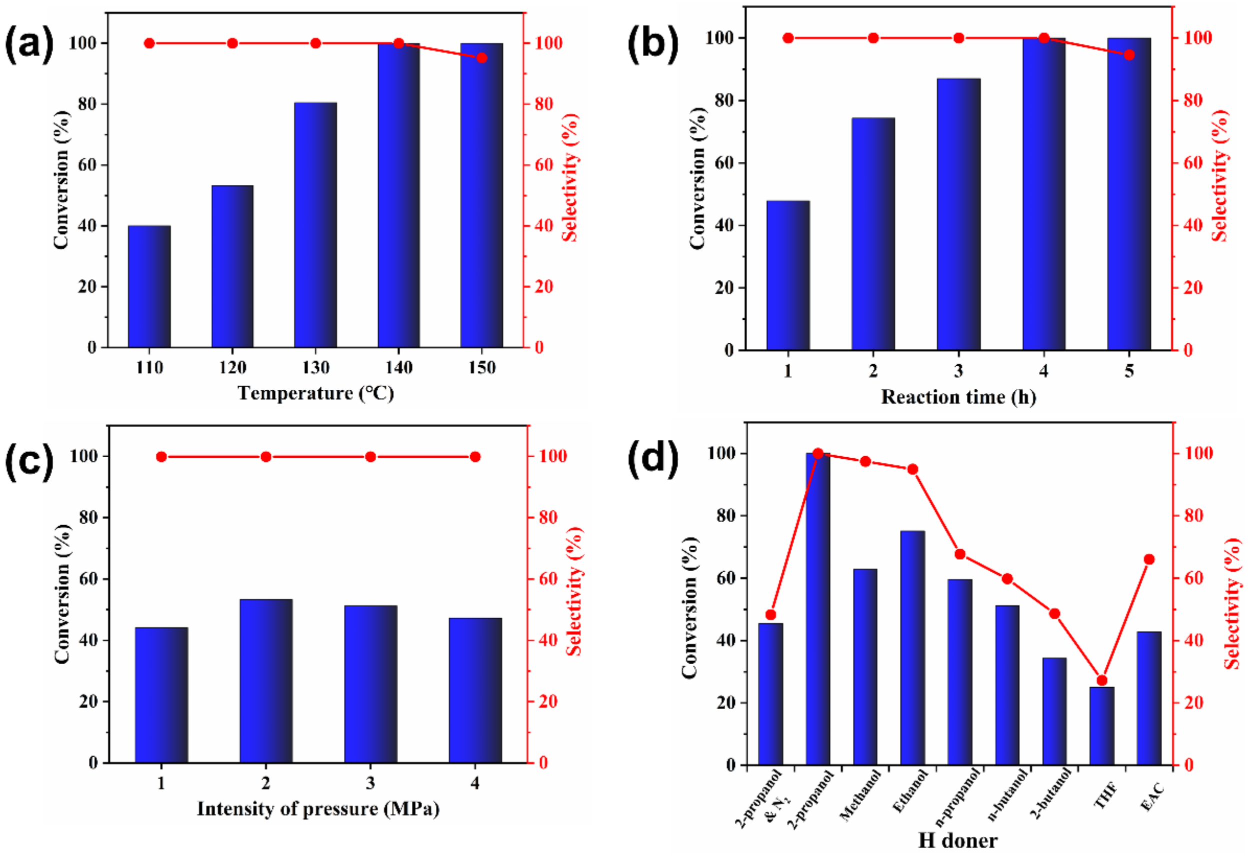

Figure S11. Effect of reaction conditions on hydrogenation of EL to GVL over Co_3Zn_1@NPC-600: (a) EL (144 mg), catalyst (0.025 g), 2-propanol (8 mL), 2 MPa H_2, 4 h; (b) EL (144 mg), catalyst (0.025 g), 2-propanol (8 mL), 2 MPa H_2, 140 °C; (c) EL (144 mg), catalyst (0.025 g), 2-propanol (8 mL), 140 °C, 4 h; (d) EL (144 mg), catalyst (0.025 g), solvent (8 mL), 4h, 2 MPa H_2 and 140 °C (2 MPa N_2 and 160 °C).

Supplementary Tables

Table S1. The XPS element analysis of Co_xZn_y@NPC-T samples.

Sample	% C	% N	% Co	% Zn
Zn@NPC-600	89.20	3.27	0.00	7.53
Co_1Zn_3@NPC-600	84.98	6.74	2.23	6.05
Co_1Zn_1@NPC-600	84.82	7.45	2.41	5.32
Co_3Zn_1@NPC-600	82.91	9.37	2.60	5.12
Co_5Zn_1@NPC-600	82.54	9.64	2.73	5.09
$Co_{11}Zn_1$@NPC-600	81.69	10.47	2.81	5.03
Co@NPC-600	81.17	15.68	3.15	0.00
Co_3Zn_1@NPC-500	84.94	7.29	2.46	5.31
Co_3Zn_1@NPC-700	87.58	4.61	2.97	4.84
Co_3Zn_1@NPC-800	88.37	3.91	3.42	4.30

Table S2. N Surface chemical compositions [a] and metal loadings [b] of Co_xZn_y@NPC-T materials.

Sample	Pyridinic N 398.8 eV	Pyrrolic N 399.8 eV	Graphite N 401.1 eV	Oxidized N 403.0 eV	Co (wt %)	Zn (wt %)
Zn@NPC-600	18.60	36.34	22.12	22.94	—	18.29
Co_1Zn_3@NPC-600	21.71	45.59	30.14	2.57	11.31	15.07
Co_1Zn_1@NPC-600	48.14	32.37	14.47	5.02	12.90	12.70
Co_3Zn_1@NPC-600	37.26	40.55	15.76	6.43	16.07	5.74
Co_5Zn_1@NPC-600	42.77	28.27	20.81	8.15	20.50	4.86
$Co_{11}Zn_1$@NPC-600	49.26	26.68	17.66	6.40	30.20	2.81
Co@NPC-600	28.61	54.40	7.49	9.50	32.10	—
Co_3Zn_1@NPC-500	24.57	45.63	23.8	6.00	15.56	6.56
Co_3Zn_1@NPC-700	15.17	51.05	24.47	9.30	17.10	2.05
Co_3Zn_1@NPC-800	3.07	53.64	29.10	14.18	18.90	0.90

[a] Investigated by XPS analysis. [b] Detected by ICP-OES.

Table S3. The amounts of acidic sites by NH_3-TPD test.

Entry	Catalyst	Quantity at 138 ℃ (cm^3 / g)	Quantity at 483 ℃ (cm^3 / g)	Total Quantity (cm^3 / g)
1	Co_1Zn_3@NPC-600	23.18	15.41	38.59
2	Co_3Zn_1@NPC-600	21.14	16.89	38.03
3	$Co_{11}Zn_1$@NPC-600	19.87	12.88	32.75

Table S4. The H_2-TPD result of Co_3Zn_1@NPC-600 and Co@NPC-600 catalyst.

Entry	Catalyst	Peak temperature (℃)	Amount of desorbed H_2 (mmol / g)	Peak temperature (℃)	Amount of desorbed H_2 (mmol / g)	Peak temperature (℃)	Amount of desorbed H_2 (mmol / g)
1	Co_3Zn_1@NPC-600	167	0.059	517	0.479	768	0.740
2	Co@NPC-600	167	0.079	480	0.231	799	0.613

Table S5. Hydrogenation of EL to GVL over comparative catalysts.

Entry	Catalyst	Con (%)	Sel (%)	Yie (%)
1	Co_3Zn_1@NPC-600	100	>99	>99
2	Co_3Zn_1@NPC-600(NH_4Cl)	6.8	69.1	4.7

Reaction conditions: EL, 144 mg; catalyst, 0.025 g; 2-propanol, 8 mL; H_2, 2 MPa; 140 ℃; 4 h.

Table S6. Comparison of the EL hydrogenation performance over the Co_3Zn_1@NPC-600 catalyst with some other catalysts reported for this reaction.

Catalyst	Reaction condition	Conversion (%)	Selectivity (%)	Reference
2.8Cu-3.5Fe/SBA-15	150 ℃, 3 MPa H_2, 3 h	97.0	>99.0	5
CuMgAl-1-1	140 ℃, 6 MPa H_2, 6 h	100	>99.0	6
2.1Co-0.9Mg-Al	150 ℃, 3 MPa H_2, 2 h	97.0	>99.0	7
CNT-Ru-1	60 ℃, 3 MPa H_2, 6 h	99.0	87.0	8
Ni/AC	150 ℃, 1 MPa H_2, 12 h	99.7	79.8	9
Ni-SAs/NC	180 ℃, 2 MPa H_2, 3 h	81.8	63.9	10
Co(glycerin)	150 ℃, 3 MPa H_2, 4 h	82.9	60.1	11
Co_3Zn_1@NPC-600	140 ℃, 2 MPa H_2, 4 h	100	>99.0	This work

References

1. Kresse, G.; Furthmüller, J., Efficiency of Ab-Initio Total Energy Calculations for Metals and Semiconductors Using a Plane-Wave Basis Set. *Comput. Mater. Sci.* **1996,** *6* (1), 15-50.

2. Kresse, G.; Furthmüller, J., Efficient Iterative Schemes for Ab Initio Total-Energy Calculations Using a Plane-Wave Basis Set. *Phys. Rev. B* **1996,** *54* (16), 11169-11186.

3. Perdew, J. P.; Burke, K.; Ernzerhof, M., Generalized Gradient Approximation Made Simple. *Phys. Rev. Lett.* **1996,** *77* (18), 3865-3868.

4. Grimme, S., Semiempirical GGA-type Density Functional Constructed with a Long-Range Dispersion Correction. *J. Comput. Chem.* **2006,** *27* (15), 1787-1799.

5. Deng, T.; Yan, L.; Li, X.; Fu, Y., Continuous Hydrogenation of Ethyl Levulinate to 1,4-Pentanediol over 2.8Cu-3.5Fe/SBA-15 Catalyst at Low Loading: The Effect of Fe Doping. *ChemSusChem* **2019,** *12* (16), 3837-3848.

6. Shao, Y.; Sun, K.; Li, Q.; Liu, Q.; Zhang, S.; Liu, Q.; Hu, G.; Hu, X., Copper-Based Catalysts with Tunable Acidic and Basic Sites for the Selective Conversion of Levulinic Acid/Ester to γ-Valerolactone or 1,4-Pentanediol. *Green Chem.* **2019,** *21* (16), 4499-4511.

7. Shao, Y.; Ba, S.; Sun, K.; Gao, G.; Fan, M.; Wang, J.; Fan, H.; Zhang, L.; Hu, X., Selective Production of γ-Valerolactone or 1,4-Pentanediol from Levulinic Acid/Esters over Co-based Catalyst: Importance of the Synergy of Hydrogenation Sites and Acidic sites. *Chem. Eng. J.* **2022,** *429*, 132433.

8. Shen, Q.; Zhang, Y.; Zhang, Y.; Tan, S.; Chen, J., Transformations of Biomass-Based Levulinate Ester into γ-Valerolactone and Pyrrolidones Using Carbon Nanotubes-Grafted N-Heterocyclic Carbene Ruthenium Complexes. *J. Energy Chem.* **2019,** *39*, 29-38.

9. Ji, N.; Liu, Z.; Diao, X.; Bao, J.; Yu, Z.; Song, C.; Liu, Q.; Ma, D.; Lu, X., A Novel Ni/AC Catalyst Prepared by MOCVD Method for Hydrogenation of Ethyl Levulinate to γ-Valerolactone. *Mol. Catal.* **2020,** *495*.

10. Fan, Y.; Zhuang, C.; Li, S.; Wang, Y.; Zou, X.; Liu, X.; Huang, W.; Zhu, G., Efficient Single-Atom Ni for Catalytic Transfer Hydrogenation of Furfural to Furfuryl Alcohol. *J. Mater. Chem. A* **2021,** *9* (2), 1110-1118.

11. Zhao, H.; Hao, J.; Ban, Y.; Sha, Y.; Zhou, H.; Liu, Q., Novel and Efficient Cobalt Catalysts Synthesized by One-Step Solution Phase Reduction for the Conversion of Biomass Derived Ethyl Levulinate. *Catal. Today* **2019,** *319*, 145-154.